# Quantum spin dynamics with pairwise-tunable, long-range interactions

C.-L. Hung[a,b,1,2], Alejandro González-Tudela[c,1,2], J. Ignacio Cirac[c], and H. J. Kimble[c,d,e,2]

[a]Department of Physics and Astronomy, Purdue University, West Lafayette, IN 47907; [b]Purdue Quantum Center, Purdue University, West Lafayette, IN 47907; [c]Max-Planck-Institut für Quantenoptik, 85748 Garching, Germany; [d]Norman Bridge Laboratory of Physics, California Institute of Technology, Pasadena, CA 91125; and [e]Institute for Quantum Information and Matter, California Institute of Technology, Pasadena, CA 91125

Contributed by H. Jeffrey Kimble, June 19, 2016 (sent for review March 6, 2016; reviewed by Nathan Goldman and Ana Maria Rey)

**We present a platform for the simulation of quantum magnetism with full control of interactions between pairs of spins at arbitrary distances in 1D and 2D lattices. In our scheme, two internal atomic states represent a pseudospin for atoms trapped within a photonic crystal waveguide (PCW). With the atomic transition frequency aligned inside a band gap of the PCW, virtual photons mediate coherent spin–spin interactions between lattice sites. To obtain full control of interaction coefficients at arbitrary atom–atom separations, ground-state energy shifts are introduced as a function of distance across the PCW. In conjunction with auxiliary pump fields, spin-exchange versus atom–atom separation can be engineered with arbitrary magnitude and phase, and arranged to introduce nontrivial Berry phases in the spin lattice, thus opening new avenues for realizing topological spin models. We illustrate the broad applicability of our scheme by explicit construction for several well-known spin models.**

nanophotonics | quantum matter | cold atoms | quantum many-body | quantum spin

Quantum simulation has become an important theme for research in contemporary physics (1). A quantum simulator consists of quantum particles (e.g., neutral atoms) that interact by way of a variety of processes, such as atomic collisions. Such processes typically lead to short-range, nearest-neighbor interactions (2–6). Alternative approaches for quantum simulation use dipolar quantum gases (7, 8), polar molecules (9–11), and Rydberg atoms (12–15), leading to interactions that typically scale as $1/r^3$, where $r$ is the interparticle separation. For trapped ion quantum simulators (16–20), tunability in a power law scaling of $r^{-\eta}$ with $0<\eta<3$ can in principle be achieved. Beyond simple power law scaling, it is also possible to engineer arbitrary long-range interactions mediated by the collective phonon modes, which can be achieved by independent Raman addressing on individual ions (21).

Using photons to mediate controllable long-range interactions between isolated quantum systems presents yet another approach for assembling quantum simulators (22). Recent successful approaches include coupling ultracold atoms to a driven photonic mode in a conventional mirror cavity, thereby creating quantum many-body models (using atomic external degrees of freedom) with cavity-field–mediated infinite-range interactions (23). Finite-range and spatially disordered interactions can be realized by using multimode cavities (24). Recent demonstrations on coupling cold atoms to guided mode photons in photonic crystal waveguides (25, 26) and cavities (27, 28) present promising avenues (using atomic internal degrees of freedom) due to unprecedented strong single atom–photon coupling rate and scalability. Related efforts also exists for coupling solid-state quantum emitters, such as quantum dots (29, 30) and diamond nitrogen-vacancy centers (31, 32), to photonic crystals. Scaling to a many-body quantum simulator based on solid-state systems, however, still remains elusive. Successful implementations can be found in the microwave domain, where superconducting qubits behave as artificial atoms strongly coupled to microwave photons propagating in a network formed by superconducting resonators and transmission lines (33–35).

Here, we propose and analyze a physical platform for simulating long-range quantum magnetism in which full control is achieved for the spin-exchange coefficient between a pair of spins at arbitrary distances in 1D and 2D lattices. The enabling platform, as described in refs. 36 and 37, is trapped atoms within photonic crystal waveguides (PCWs), with atom–atom interactions mediated by photons of the guided modes (GMs) in the PCWs. As illustrated in Fig. 1 *A* and *B*, single atoms are localized within unit cells of the PCWs in 1D and 2D periodic dielectric structures. At each site, two internal atomic states are treated as pseudospin states, with spin-1/2 considered here for definiteness (e.g., states $|g\rangle$ and $|s\rangle$ in Fig. 1*C*).

Our scheme uses strong, and coherent atom–photon interactions inside a photonic band gap (36–40), and long-range transport property of GM photons for the exploration of a large class of quantum magnetism. This is contrary to conventional hybrid schemes based on, for example, arrays of high finesse cavities (41–44) in which the pseudospin acquires only the nearest (or at most the next-nearest) neighbor interactions due to strong exponential suppression of photonic wave packet beyond single cavities.

In its original form (36–40), the localization of pseudospin is effectively controlled by single-atom defect cavities (36). The cavity mode function can be adjusted to extend over long distances within the PCWs, thereby permitting long-range spin exchange interactions. The interaction can also be tuned dynamically, via external addressing beams, to induce complex long-range spin transport, which we describe in the following (36, 37).

To engineer tunable, long-range spin Hamiltonians, we use an atomic $\Lambda$ scheme and two-photon Raman transitions, where an atom flips its spin state by scattering one photon from an external pump field into the GMs of a PCW. The GM photon then propagates within the waveguide, inducing spin flip in an atom located at a

## Significance

**Cold atoms trapped along a photonic crystal waveguide can be used to simulate long-range quantum magnetism with pairwise-tunable spin–spin interactions mediated by guided virtual photons in a photonic band gap. Using a two-photon Raman addressing scheme, the proposed atom-nanophotonic system can achieve arbitrary and dynamic control on the strength, phase, and length scale of spin interactions. This promises new avenues for engineering a large class of spin Hamiltonians, including those exhibiting topological order or frustrated long-range magnetism.**

Author contributions: C.-L.H. developed concept and analytical calculations; C.-L.H., A.G.-T., J.I.C., and H.J.K. performed research; C.-L.H., A.G.-T., J.I.C., and H.J.K. contributed materials; A.G.-T. performed analytical and numerical analysis; and C.-L.H., A.G.-T., and H.J.K. wrote the paper.

Reviewers: N.G., Université libre de Bruxelles; and A.M.R., JILA, University of Colorado.

The authors declare no conflict of interest.

Freely available online through the PNAS open access option.

[1]C.-L.H. and A.G.-T. contributed equally to this work.

[2]To whom correspondence may be addressed. Email: hjkimble@caltech.edu, clhung@purdue.edu, or alejandro.gonzalez-tudela@mpq.mpg.de.

This article contains supporting information online at www.pnas.org/lookup/suppl/doi:10.1073/pnas.1603777113/-/DCSupplemental.

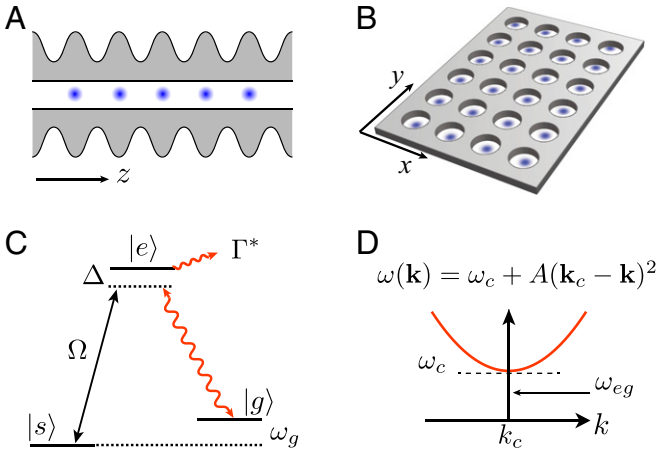


**Fig. 1.** Photon-mediated atom–atom interactions in (*A*) 1D and (*B*) 2D PCWs. (*C*) Atomic-level scheme: atomic dipole $|s\rangle \leftrightarrow |e\rangle$ is coupled to an external pump, $|g\rangle \leftrightarrow |e\rangle$ coupled to a GM photon, and $\Gamma^*$, the excited state decay rate to free space and leaky modes.† (*D*) Simplified band structure $\omega(\mathbf{k})$ near the band edge $\mathbf{k} = \mathbf{k}_c$ and $\omega(\mathbf{k}_c) = \omega_c$. Atomic transition frequency $\omega_{eg} = \omega_e - \omega_g$ lies within the band gap.

distant site via the reverse two-photon Raman process. When we align the atomic resonant frequency inside the photonic band gap, as depicted in Fig. 1*D*, only virtual photons can mediate this remote spin exchange and the GM dynamics are fully coherent, effectively creating a spin Hamiltonian with long-range interactions. As discussed in refs. 36 and 37, the overall strength and length scale of the spin-exchange coefficients can be tuned by an external pump field, albeit within the constraints set by a functional form that depends on the dimensionality and the photonic band structure. These constraints may limit our ability to explore novel quantum phases and nonequilibrium dynamics in various spin models, because many effects display strong dependencies on the functional form of long-range interactions (45–50). It is therefore highly desirable to obtain full control of interactions without the need to investigate over a wide range of PCW designs with different photonic band structures.

To fully control spin-exchange coefficients at arbitrary separations, here we adopt a Raman-addressing scheme similarly discussed for cold atoms and trapped ions (51–55). We introduce atomic ground-state energy shifts as a function of distance across the PCW. Due to conservation of energy, these shifts suppress reverse two-photon Raman processes in the original scheme (36, 37), forbidding spin exchange within the entire PCW. However, we can selectively activate certain spin-exchange interactions $J(r_{m,n})$ between atom pairs $(m,n)$ separated by $r_{m,n}$, by applying an auxiliary sideband whose frequency matches that of the original pump plus the ground-state energy shift between the atom pairs. This allows us to build a prescribed spin Hamiltonian with interaction terms "one by one." Note that each sideband in a Raman-addressing beam can be easily introduced, for example, by an electro-optical modulator. By introducing multiple sidebands and by controlling their frequencies, amplitudes, and relative phases, we can engineer spin Hamiltonians with arbitrary, complex interaction coefficients $J(r_{m,n})$. Depending on the dimensionality and the type of spin Hamiltonians, our scheme requires only one or a few Raman beams to generate the desired interactions. Furthermore, by properly choosing the propagation phases of the Raman beams, we can imprint geometric phases in the spin system, thus providing unique opportunities for realizing topological spin models.

We substantiate the broad applicability of our methods by explicit elaboration of the set of pump fields required to realize well-known spin Hamiltonians. For 1D spin chains, we consider the implementation of the Haldane–Shastry model (56, 57). For 2D spin lattices, we elaborate the configurations for realizing topological flat bands (58, 59) in Haldane's spin model (56), as well as a "checkerboard" chiral-flux lattice (58, 59). We also consider a 2D *XXZ* spin Hamiltonian with $J(r_{m,n}) \propto 1/r_{m,n}^{\eta}$ and $\eta = 1,2,3$ (60). In addition, we report numerical results on the $\eta$ dependence of its magnetization diagram.

## Controlling Spin–Spin Interaction Through Multifrequency Driving

In the following, we discuss how to achieve full control of interactions by multifrequency pump fields. We assume (*i*) $N$ atoms trapped in either a 1D or 2D PCW, as depicted in Fig. 1 *A* and *B*, with a spatially dependent ground-state energy shift $\omega_g$. For simplicity, we assume one atom per unit cell of the PCW, although this assumption can be relaxed afterward; (*ii*) the structure is engineered (22–28) such that the GM polarization is coupled to the atomic dipole, $|g\rangle \leftrightarrow |e\rangle$, as shown in Fig. 1*C*, and, under rotating wave approximation, is described by the following Hamiltonian (using $\hbar = 1$):

$$H_{\rm lm} = \sum_{\mathbf{k},n} g_{\mathbf{k}}(\mathbf{r}_n) a_{\mathbf{k}} \sigma_{eg}^n + \text{h.c.}, \qquad [1]$$

where $g_{\mathbf{k}}(\mathbf{r}_n) = g_{\mathbf{k}} e^{i\mathbf{k}\cdot\mathbf{r}_n}$ is the single-photon coupling constant at site location $\mathbf{r}_n$, with $n$ being the site index; $a_{\mathbf{k}}$, the GM field operator; and $\sigma_{ab}^n \equiv |a\rangle_n\langle b|$, the atomic operators with $a, b$ being one of the $g, s, e$ states. Moreover, as in refs. 36 and 37, we assume (*iii*) there is another hyperfine level $|s\rangle$, addressed by a Raman field with coupling strength $\Omega$ as follows:

$$H_{\rm d}(t) = \sum_n \left( \frac{\Omega(t)}{2} \sigma_{se}^n e^{i\omega_L t} + \text{h.c.} \right), \qquad [2]$$

where $\omega_L$ is the main driving frequency. The Raman field $\Omega(t)$ contains $m_P$ frequency components that are introduced to achieve full control of the final effective spin Hamiltonian. Full dependence of $\Omega(t)$ can be written as follows:

$$\Omega(t) \equiv \sum_{\alpha=0}^{m_p-1} \Omega_\alpha e^{i\tilde{\omega}_\alpha t}, \qquad [3]$$

where $\tilde{\omega}_\alpha$ are the detunings of the sidebands from the main frequency $\omega_{\rm L}$ such that $\tilde{\omega}_0 = 0$, and $\Omega_\alpha$, the complex amplitudes.

We can adiabatically eliminate the excited states $|e\rangle$ and the photonic GMs under the condition that (*iv*) $\max\{|\Omega|, |\tilde{\omega}_\alpha - \tilde{\omega}_\beta|\} \ll |\Delta| = |\omega_e - \omega_{\rm L}|$. This condition guarantees that, first, the excited state is only virtually populated, and that, second, the time dependence induced by the sideband driving is approximately constant over the timescale $\Delta^{-1}$. As discussed in refs. 36 and 37, if $\omega_L - \omega_g$ lies in the photonic band gap, photon-mediated interactions by GMs are purely coherent.† Under the Born–Markov approximation, we then arrive at an effective *XY* Hamiltonian (*SI Appendix A: Complete Derivation of Final Time-Dependent Hamiltonian*):

$$H_{XY}(t) = \sum_{m,n\neq m}^{N} \sum_{\alpha,\beta=0}^{m_P-1} X_\alpha X_\beta^* \tilde{J}(\mathbf{r}_{m,n}) e^{i\left(\omega_{g,m} - \omega_{g,n} + \tilde{\omega}_\alpha - \tilde{\omega}_\beta\right)t} \sigma_{gs}^m \sigma_{sg}^n, \qquad [4]$$

where we have defined $X_\alpha = \Omega_\alpha/(2\Delta)$; $\omega_{g,n} = \omega_g(\mathbf{r}_n)$ is the site-dependent ground-state energy shift, and $\tilde{J}(\mathbf{r}_{m,n})$ is the atom-GM photon coupling strength (36, 37) that typically depends on atomic separation $\mathbf{r}_{m,n} = \mathbf{r}_m - \mathbf{r}_n$.

We focus on "sideband engineering" and treat $\tilde{J}(\mathbf{r}_{m,n})$ as approximately constant over atomic separations considered.‡ This is valid as long as the farthest atomic separation with nonzero engineered interaction is much smaller than the decay length

†To simplify the discussion, in this paper, we neglect decoherence effects caused by atomic emission into free space and leaky modes as well as photon loss due to imperfections in the PCW. These effects were both carefully discussed in refs. 36 and 37, suggesting the number of spin-exchange cycles in the presence of decoherence can realistically reach $\mathcal{N} \approx 35 \sim 100$ using ultra-high Q PCWs.

‡One may also replace a PCW with a single-mode nanophotonic cavity, operating in the strong dispersive regime (61, 62), to achieve constant GM coupling $\tilde{J}$ independent of $|\mathbf{r}_{m,n}|$. Realistic nanophotonic cavity implementations will be considered elsewhere.

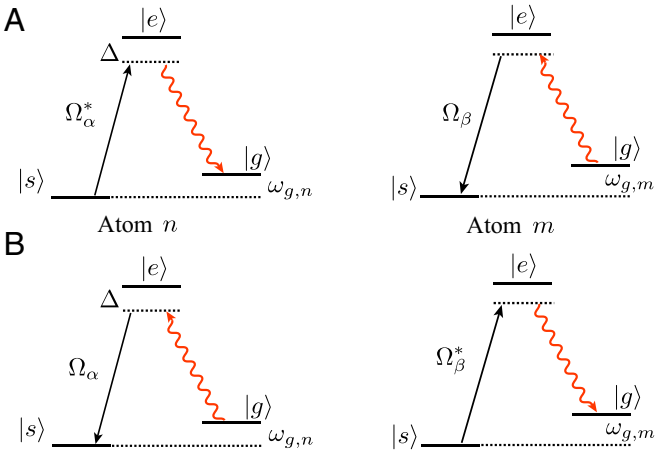


**Fig. 2.** Schematics to engineer long-range spin exchange interactions via resonant Raman-scattering processes. Spin exchanges (*A*) $|s_n, g_m\rangle \to |g_n, s_m\rangle$ and (*B*) $|g_n, s_m\rangle \to |s_n, g_m\rangle$ are allowed only when the condition $\omega_{g,m} - \omega_{g,n} = \tilde{\omega}_\beta - \tilde{\omega}_\alpha$ is satisfied. $\Omega_\alpha/\Delta$ and $\Omega_\beta/\Delta$ control the exchange rate.

scale $\xi = \sqrt{|A/\Delta_c|}$ of the coupling strength $\tilde{J}(\mathbf{r}_{m,n})$. Here, $A$ is the band curvature (Fig. 1*D*), $\Delta_c = \max\{\omega_c - (\omega_L - \omega_{g,n})\}$ is the maximal detuning of the band edge to the frequency of coupled virtual photons that mediate interactions (Fig. 1*C*), and we have assumed that the variation of ground-state energies $\omega_{g,n}$ are small compared with $\Delta_c$. Exact functional form of $\tilde{J}(\mathbf{r}_{m,n})$ can be found in refs. 36 and 37, and in *SI Appendix A: Complete Derivation of Final Time-Dependent Hamiltonian*.

The time dependence in Eq. 4 can be further engineered and simplified. We note that the interaction between two atoms $n$ and $m$ will be highly dependent on the resonant condition $\omega_{g,m} - \omega_{g,n} = \tilde{\omega}_\beta - \tilde{\omega}_\alpha$, provided the ground-state energy difference $|\omega_{g,n} - \omega_{g,m}|$ is much larger than the characteristic timescale of interactions $|X_\alpha X^*_\beta \tilde{J}|$. The intuitive picture is depicted in Fig. 2*A*: the atom $n$ scatters from sideband $\alpha$ a photon with energy $\omega_L + \tilde{\omega}_\alpha - \omega_{g,n}$ into the GMs. When this GM photon propagates to the atom $m$, it will only be rescattered into a sideband $\beta$ that satisfies $\omega_L + \tilde{\omega}_\alpha - \omega_{g,n} = \omega_L + \tilde{\omega}_\beta - \omega_{g,m}$, whereas the rest of the sidebands remain off-resonant. Fig. 2*B* depicts a reversed process.

For concreteness, we discuss a 1D case where we assume ($v$) a linear gradient in the ground-state energy $\omega_{g,n} \equiv n\delta$, with $\delta$ being the energy difference between adjacent sites. The sidebands will be chosen accordingly such that $\tilde{\omega}_\alpha = \alpha\delta$, with $\alpha \in \mathbb{Z}$.

Summing up, with all these assumptions (*i*–*v*), the resulting effective Hamiltonian Eq. **4** can finally be rewritten as follows:

$$H_{XY}(t) = \sum_p H_{XY,p}\, e^{ip\delta t}, \qquad [5]$$

where $H_{XY,p}$ is the contribution that oscillates with frequency $p\delta$. Written explicitly,

$$H_{XY,p} = \sum_{m,n\neq m}^{N} \sum_{\alpha,\beta=0}^{m_P-1} X_\alpha X^*_\beta \tilde{J} \delta_{n-m,\beta-\alpha-p} \sigma^m_{gs} \sigma^n_{sg}. \qquad [6]$$

In an ideal situation, the gradient per site satisfies $\delta \gg |X_\alpha X^*_\beta \tilde{J}|$ such that the contributions from $H_{XY,p}\ \forall\, p \neq 0$ can be neglected. Under these assumptions, we arrive at an effective time-independent Hamiltonian:

$$H_{XY}(t) \approx H_{XY,0} = \sum_{m,n\neq m}^{N} J_{m,n} \sigma^m_{gs} \sigma^n_{sg}, \qquad [7]$$

where couplings $J_{m,n}$ can be tuned by adjusting the amplitudes and phases of the sidebands $X_\alpha$ as they are given by the following:

$$J_{m,n} = \sum_{\alpha,\beta=0}^{m_P-1} X_\alpha X^*_\beta \tilde{J} \delta_{n-m,\beta-\alpha}. \qquad [8]$$

It can be shown that the set of equations defined by Eq. **8** has at least one solution for any arbitrary choice of $J_{m,n}$, that is, by choosing $\Omega_0 \gg \Omega_{\alpha\neq 0}$ and $J_{m,n} \approx (X_0 X^*_{n-m} + X^*_0 X_{m-n})\tilde{J}$. More solutions can be found by directly solving the set of nonlinear equations Eq. **8**.

It is important to highlight that multifrequency driving also enables the possibility to engineer geometrical phases and, therefore, topological spin models. If the pump field propagation is not perfectly transverse, that is, $\mathbf{k}_L \cdot \mathbf{r}_{m(n)} \neq 0$ ($\mathbf{k}_L$ being the wave vector of the Raman field), the effective Hamiltonian Eq. **7** acquires spatial-dependent, complex spin-exchange coefficients via the phase of $X_\alpha X^*_\beta$ in Eq. **8**; see later discussions.

Beyond an ideal setting, we now stress a few potential error sources. First, for practical situations, the gradient per site $\delta$ will be a limited resource, making Eq. **7** not an ideal approximation. Careful Floquet analysis on time-dependent Hamiltonian in Eqs. **5** and **6** is required, to be discussed later. Second, there is an additional Stark shift on state $|s\rangle$ due to the Raman fields:

$$\delta\omega_s(t) = -\sum_{\alpha=0}^{m_P-1} \frac{|\Omega_\alpha|^2}{4\Delta} - \sum_{\alpha>\beta}^{m_P-1} \Re\left[\frac{\Omega_\alpha \Omega^*_\beta}{2\Delta} e^{i(\tilde{\omega}_\alpha - \tilde{\omega}_\beta)t}\right], \qquad [9]$$

where $\Re[.]$ indicates real part. We note that the time-independent contribution in Eq. **9** can be absorbed into the energy of $\omega_s$ without significant contribution to the dynamics, whereas the time-dependent terms may be averaged out over the atomic timescales that we are interested in. We will present strategies for optimizing the choice of $\delta$, and minimizing detrimental effects due to undesired time-dependent terms in Eqs. **5** and **9** in later discussions.

**Independent Control of *XX* and *YY* Interactions.** So far, we can fully engineer an *XY* Hamiltonian with equal weight between *XX* and *YY* terms by defining the Pauli operators $(\sigma_x, \sigma_y, \sigma_z) = (\sigma_{sg} + \sigma_{gs}, i(\sigma_{sg} - \sigma_{gs}), \sigma_{gg} - \sigma_{ss})$. We now show flexible control of *XX* and *YY* interactions with slight modifications in the atomic level structure and the Raman-addressing scheme. In particular, we use a butterfly-like level structure where there are two transitions, $|g\rangle \leftrightarrow |e\rangle$ and $|s\rangle \leftrightarrow |\tilde{e}\rangle$, coupled to the same GM, as depicted in Fig. 3. We will use two multifrequency Raman pump fields, $\Omega_g(t)$ and $\Omega_s(t)$, to induce $|g\rangle \leftrightarrow |\tilde{e}\rangle \leftrightarrow |s\rangle$ and $|s\rangle \leftrightarrow |e\rangle \leftrightarrow |g\rangle$ two-photon Raman transitions, respectively.

For example, to control *XX* or *YY* interactions, we require that the two pump fields induce spin flips with equal amplitude, that is, $\sigma_{gs} \pm \sigma_{sg}$. This is possible if we choose the main frequencies of the pumps ($\omega_{L,g}$ and $\omega_{L,s}$) such that $\omega_{L,s} = \omega_{L,g} + 2\omega_g$, and match their amplitudes such that $|\Omega_{g,\alpha}|/\Delta_g = |\Omega_{s,\alpha}|/\Delta_s$, where $\Delta_s = \omega_e - \omega_{L,s}$, $\Delta_g = \omega_{\tilde{e}} - (\omega_{L,g} + \omega_g)$, and $|\Delta_{s,g}| \gg |\Omega_{s,g}|$.

Adiabatically eliminating the excited states as well as the GMs, we arrive at the following Hamiltonian:

$$H_{XX,YY,0} = \sum_{m,n>m}^{N} \left[J_{m,n}\left(\sigma^m_{gs} + e^{i\phi_{gs}}\sigma^m_{sg}\right)\left(\sigma^n_{sg} + e^{-i\phi_{gs}}\sigma^n_{gs}\right) + \text{h.c.}\right], \qquad [10]$$

where $\phi_{gs}$ is the relative phase between the pumps fields $\Omega_{g,s}$. Assuming the laser beams that generate the Raman fields are copropagating or are both illuminating the atoms transversely, that is, $\mathbf{k}_L \cdot \mathbf{r}_{m,n} = 0$, we can generate either *X* or *Y* components, $(\sigma^m_{sg} \pm \sigma^m_{gs})$, by setting the phase $\phi_{gs} = 0$ or $\pi$; more exotic combinations are available with generic choice of $\phi_{gs}$. Moreover, if the laser beams are not copropagating, they create spatially dependent phases $\phi_{gs,m}$. This can create site-dependent *XX*, *YY*, or *XY* terms.

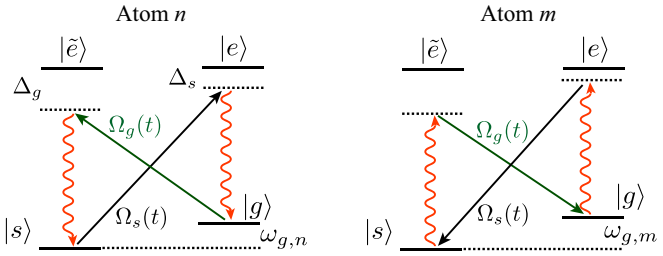


**Fig. 3.** Atomic "butterfly" level structure. Two pump fields $\Omega_s$ and $\Omega_g$, tuned to couple to the same GM photon, are introduced to control *XX* and *YY* interactions independently.

**Independent Control of *ZZ* Interactions.** An independently controlled *ZZ* Hamiltonian, in combination with arbitrary *XY* terms, would allow us to engineer SU(2)-invariant spin models as well as a large class of *XXZ* models, that is, the following:

$$H_{XXZ} = H_{XY} + H_{ZZ} = \sum_{m,n>m}^{N} \left[ \left( 2J^{xy}_{m,n} \sigma^m_{gs} \sigma^n_{sg} + \text{h.c.} \right) + J^z_{m,n} \sigma^m_z \sigma^n_z \right]. \quad [11]$$

In refs. 36 and 37, it was shown that *ZZ* interaction can be created by adding an extra pump field to the $|g\rangle \leftrightarrow |e\rangle$ transition in Fig. 1*C*. However, as *ZZ* terms in this scheme (36, 37) do not involve flipping atomic states, it is not directly applicable to our multifrequency pump method. Nonetheless, because we can generate *XX* and *YY* interactions independently, a straightforward scheme to engineer $H_{ZZ}$ is to use single qubit rotations to rotate the spin coordinates $X \leftrightarrow Z$ or $Y \leftrightarrow Z$, followed by stroboscopic evolutions (63) to engineer the full-spin Hamiltonian. Spin-rotation can be realized, for example, with a collective microwave driving $H_{\text{mw}} = \sum_n ((\Omega_{\text{mw}}/2)\sigma^n_{sg} + \text{h.c.})$, in which a $\pi/2$-microwave pulse rotates the basis $\{|g\rangle_n, |s\rangle_n\} \to \{(|g\rangle_n + |s\rangle_n)/\sqrt{2}, (-|g\rangle_n + |s\rangle_n)/\sqrt{2}\}$.

Thus, an $H_{\text{XXZ}}$ Hamiltonian can be simulated using the following stroboscopic evolution: $\{H_{XY}, H_{ZZ}, H_{XY}, H_{ZZ}, \dots\}$ in $N_t$ steps as schematically depicted in Fig. 4. As shown in *SI Appendix A: Complete Derivation of Final Time-Dependent Hamiltonian*, the error accumulated in these $N_t$ steps can be bounded by the following:

$$E_2 \le \frac{N(RJt)^2}{N_t}, \quad [12]$$

where $J = \max[J_{m,n}]$ is the largest energy scale of the Hamiltonian we want to simulate, and $R$ is the approximate number of atoms coupled through the interaction. For example, if $J_{m,n}$ is a nearest-neighbor interaction, $R = 1$. If $J_{m,n} \propto 1/|m-n|^\eta$, then $R \propto \sum_{n=1}^{N} 1/|n|^\eta$, which typically grows much slower than $N$. Because $E_2 \propto 1/N_t$, the Trotter error in $N_t$ steps can in principle be decreased to a given accuracy $\varepsilon$ by using enough steps, that is, $N_t \ge (N(RJt)^2)/\varepsilon$.

More complicated stroboscopic evolutions may lead to a more favorable error scaling (64–66), although in real experiments there will be a trade-off between minimizing the Trotter error and the fidelity of the individual operations to achieve $H_{XY}$ and $H_{ZZ}$. As this will depend on the particular experimental setup, we will leave such analysis out of current discussions. For illustration, we will only consider the simplest kind of stroboscopic evolution that we depicted in Fig. 4.

## Engineering Spin Hamiltonians for 1D Systems: The Haldane–Shastry $S = 1/2$ Spin Chain

In the first example, we engineer a Haldane–Shastry spin Hamiltonian in one dimension (56, 57):

$$H_{\text{HS}} = \sum_{m=1}^{N-1} \sum_{n=1}^{N-m} J_n \left[ 2\left( \sigma^m_{sg} \sigma^{m+n}_{gs} + \text{h.c.} \right) + \sigma^m_z \sigma^{m+n}_z \right], \quad [13]$$

where $J_n = J_0/\sin^2(n\pi/N)$, $J_0 = J\pi^2/N^2$, and $N$ is the number of spins. The interaction strength decays slowly with approximately a $1/r^2$ dependence while satisfying a periodic boundary condition. Such a spin Hamiltonian is difficult to realize in most physical setups that interact, for example, via dipolar interactions.

We can engineer the periodic boundary condition and the long-range interaction $J_n$ directly using a linear array of trapped atoms coupled to a PCW. To achieve this, we induce atomic ground-state energy shift $m\delta$ according to the spin index $m$, and then uniformly illuminate the trapped atoms with an external pump consisting of $N$ frequency components $\tilde{\omega}_\alpha = \alpha\delta$, each with an amplitude denoted by $\Omega_\alpha$ and $\alpha = 0, 1, \dots, N-1$. Regardless of the position of atoms, all pump pairs with frequency difference $n\delta$ contribute to the spin interaction $J_n$. Considering first the *XY* terms, and according to Eq. **7**, we demand the following:

$$J_n \approx \tilde{J} \sum_{\alpha=0}^{N-n-1} X_\alpha X^*_{\alpha+n} = \frac{J_0}{\sin^2(n\pi/N)}, \quad [14]$$

where $\tilde{J}$ is the GM photon coupling rate (Eq. **8**) that we will assume to be a constant for the simplicity of discussions. This requires that the physical size of the spin chain be small compared with the decay length of $\tilde{J}$. That is, $Nd \ll \xi$, where $d$ is the atomic separation. It is then straightforward to find the required pump amplitudes $\Omega_\alpha$ (or equivalently $X_\alpha$) by solving Eq. **14** for all $n$. Notice that the system of equations Eq. **14** is overdetermined, and therefore one can find several solutions of it. However, we choose the solution that minimizes the total intensity $\sum_\alpha |\Omega_\alpha|^2$. Fig. 5 shows that the total intensity converges to a constant value for large $N$, as a result of decreasing sideband amplitudes for decreasing $1/r^2$ interaction strengths. This is confirmed in Fig. 5 as we see the growth of the ratio between maximum and minimum sideband amplitudes when $N$ increases. The same external pump configuration can also be used to induce the *ZZ* terms by applying stroboscopic procedures as discussed in the previous section.

## Engineering Spin Hamiltonians for 2D Systems: Topological and Frustrated Hamiltonians

In the following, we discuss specific examples for engineering 2D spin Hamiltonians that are topologically nontrivial. In particular, we discuss two chiral-flux lattice models that require long-range

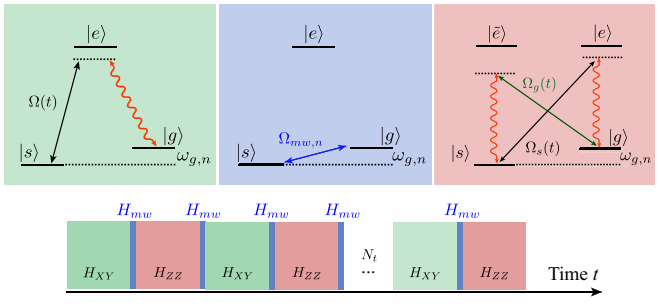


**Fig. 4.** Scheme for generating an *XXZ* spin Hamiltonian using a stroboscopic evolution. The scheme contains periodic applications of a multifrequency Raman field to induce the $H_{XY}$ interaction (in green), two fast microwave pulses (or optical two-photon transition) forming $H_{mw}$ that uniformly rotate the spin basis $\{|g\rangle_n, |s\rangle_n\} \leftrightarrow \{(|g\rangle_n + |s\rangle_n)/\sqrt{2}, (|g\rangle_n - |s\rangle_n)/\sqrt{2}\}$ back and forth (in blue), and a butterfly-like pumping scheme that applies $H_{ZZ}$ in the rotated basis.

hopping terms to engineer single particle flat-bands with nonzero Chern numbers, which are key ingredients to realizing fractional quantum Hall effects (FQHEs) without Landau levels (58, 59).

In recent years, the field of ultracold atoms has made remarkable progress in engineering topological quantum matter. An artificial gauge field (67) has been realized using cold atoms loaded into shaken optical lattices (68, 69) as well as in lattices with laser-induced tunneling (55, 54, 70–72). Various topological models, including Haldane's honeycomb lattice (73, 74), have been successfully implemented. Berry curvature and topological invariants such as the Chern number (74–80) can be measured. Chiral edge currents in synthetic quantum Hall lattices are also observed (81, 82). Most of the demonstrations so far focus on probing topological band structures and single-particle physics. Realizing strongly interacting topological phases such as FQH states, however, still remains elusive. This in part is due to limited topological bandwidth-to-gap ratio, but a number of improved schemes (e.g., refs. 83 and 84) have been proposed.

Coupling cold atoms to mobile PCW photons also allows topological band engineering and band flattening. Moreover, the pseudo spin-1/2 system already interacts like hard-core bosons because individual atoms that participate in the spin-exchange process cannot be doubly excited. With the addition of tunable long-range $ZZ$ interactions, we can readily build many-body systems that should exhibit, for example, FQH and supersolid phases (85), providing a powerful route toward realizing strongly interacting topological phases.

**Chiral-Flux Square Lattice Model.** The first example discussed here can be mapped to a topological flat-band model similarly described in refs. 58, 59, and 85. The topological spin Hamiltonian is written as follows:

$$\begin{aligned} H_{\rm flat} &= H_0 + H' \\ H_0 &= t_1 \sum_{\langle m,n\rangle} e^{i\phi_{mn}} \sigma_m^\dagger \sigma_n \pm t_2 \sum_{\langle\langle m,n\rangle\rangle} \sigma_m^\dagger \sigma_n + \text{h.c} \\ H' &= t_3 \sum_{\langle\langle\langle m,n\rangle\rangle\rangle} \sigma_m^\dagger \sigma_n + \text{h.c}, \end{aligned} \qquad [15]$$

in which we define $\sigma_m^\dagger \equiv \sigma_{sg}^m$ and $\sigma_m \equiv \sigma_{gs}^m$; $\langle . \rangle$ denotes nearest neighbors (NN), and $t_1$ is the coupling coefficient, $\langle\langle . \rangle\rangle$ [$\langle\langle\langle . \rangle\rangle\rangle$] denotes [next-]next-nearest neighbors (NNN) [and NNNN, respectively] with $t_2$ [$t_3$] being the respective coupling coefficients. The NN coupling phases $\phi_{mn} = \pm\phi$ are staggered across lattice sites, where the phase factor $\phi$ is the one that breaks time reversal symmetry for $\phi \neq 0, n\pi$ (with $n \in \mathbb{Z}$). Spin exchange between next-nearest neighbors (NNN) has real coefficients $\pm t_2$ with alternating sign along the lattice checkerboard (Fig. 6). One can show that

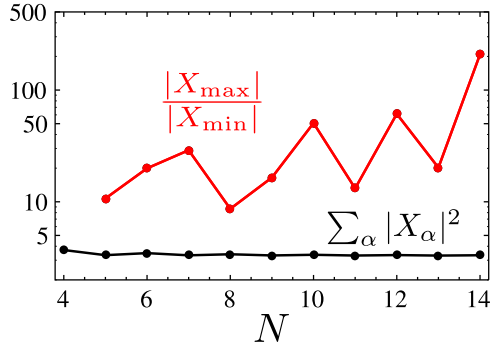


**Fig. 5.** Sideband amplitude for Haldane–Shastry model: total intensity (black) $\sum_\alpha |X_\alpha|^2$ and maximum/minimum ratio (red) of sideband amplitudes $|X_\alpha|$ as a function of $N$.

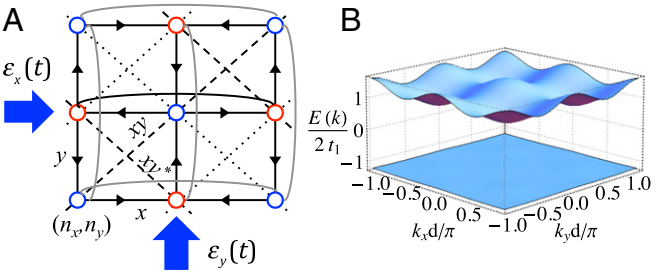


**Fig. 6.** Engineering a chiral-flux square lattice. (*A*) Two sublattices ($n_x + n_y$ odd or even) are marked by blue and red circles, respectively. Solid lines mark the NN hopping with phase gain $\phi$ (arbitrarily tuned) along the direction of the arrows. Dashed (dotted) lines mark the NNN hopping terms (coefficients $\pm t_2$). NNNN long-range hopping along curved lines are included to assist band flattening. Filled arrows indicate the propagation of pump electric fields $\varepsilon_y$ and $\varepsilon_x$, respectively; see text. (*B*) Resulting two-band structure with $(t_2, t_3, \phi) = (t_1/\sqrt{2}, t_1/4\sqrt{6}, \pi/4)$.

already $H_0$ has a small bandwidth with nontrivial Chern number that, choosing $t_2 = t_1/\sqrt{2}$ and $\phi = \pi/4$, results in a simple band dispersion $E_0(\mathbf{k}) = \pm\sqrt{2}t_1\sqrt{3+\cos(k_x+k_y)\cos(k_x-k_y)}$. Adding $H'$ to $H_0$ with, for example, $t_3 = 1/4\sqrt{6}t_1$ allows us to engineer an even flatter lower band whose bandwidth is $\sim 1$ % of the band gap.

We can use an array of atoms trapped within a 2D PCW, as in Fig. 1*B*, to engineer the Hamiltonian $H_{\rm flat}$ of Eq. **15**. For simplicity, we assume that there is one atom per site although this is not a fundamental assumption.[§] As shown in Fig. 6*A*, we need to engineer spin exchange in four different directions, namely, $\hat{x}, \hat{y}, \hat{x} \pm \hat{y}$. We first introduce linear Zeeman shifts by properly choosing a magnetic field gradient $\nabla B$ (*SI Appendix B: Proper Choice of Ground-State Energy Shifts in 2D Models*) such that $\delta_\alpha = |\mu_B \nabla B \cdot \Delta\mathbf{r}_\alpha|$, where $\mu_B$ is the magnetic moment, $\Delta\mathbf{r}_\alpha$ are vectors associated with the directions of spin exchange: $\{\Delta\mathbf{r}_\alpha\}_{\alpha=x,y,xy,xy^*} = \{d\hat{x}, d\hat{y}, d(\hat{x}+\hat{y}), d(\hat{x}-\hat{y})\}$, and $d$ is the lattice constant. To activate spin exchange along these directions while suppressing all other processes, we consider a simplest case by applying a strong pump field of amplitude $\Omega_0$ (frequency $\omega_{\rm L}$) to pair with sidebands $|\Omega_\alpha| \ll |\Omega_0|$ of detunings $\tilde{\omega}_\alpha = \delta_\alpha$ to satisfy the resonant conditions. To generate the desired chiral-flux lattice, we need to carefully consider the propagation phases $\mathbf{k}_0 \cdot \mathbf{r}_n$ ($\mathbf{k}_\alpha \cdot \mathbf{r}_n$) of the pump field (and sidebands), where $\mathbf{r}_n = d(n_x\hat{x} + n_y\hat{y})$ is the site coordinate and $n_{x,y} \in \mathbb{Z}$. In the following, we pick $k = k_\alpha = \pi/d$.

We can generate the couplings in $H_{\rm flat}$, term by term, as follows.

***Staggered NN coupling along $\Delta\mathbf{r}_{\alpha=x,y}$.*** We consider the strong pump field to be propagating along $\hat{y}$, that is, $X_0(\mathbf{r}_n) = (|\Omega_0|/2\Delta)e^{-in_y\pi}$. At the NN site $\mathbf{r}_m = \mathbf{r}_n + \Delta\mathbf{r}_x$, it can pair with an auxiliary sideband of detuning $\tilde{\omega}_x = \delta_x = |\mu_B \nabla B \cdot \Delta\mathbf{r}_x|$ with $X_x(\mathbf{r}_m) = (|\Omega_1|/2\Delta)[e^{-in_y\pi} - i\zeta e^{-i(n_x+1)\pi}]$ to generate coupling along $\Delta\mathbf{r}_x$. The sideband is formed by two field components in $\varepsilon_y(t)$ and $\varepsilon_x(t)$, propagating along $\hat{y}$ and $\hat{x}$, respectively (Fig. 6), with an amplitude ratio of $\zeta$ and with an initial $\pi/2$ phase difference. These two fields are used to independently control real and imaginary parts of the spin-exchange coefficients. Using Eq. **8** under the condition $|\Omega_0| \gg |\Omega_\alpha|$, the coupling rate along $\Delta\mathbf{r}_x$ is as follows:

$$J_{m,n} = \tilde{J} X_0 X_x^* = t_1 \frac{[1 - i\zeta(-1)^{n_x - n_y}]}{\sqrt{1+\zeta^2}} = t_1 e^{\pm i\phi}, \qquad [16]$$

where $t_1 = \tilde{J}|X_0||X_x|\sqrt{1+\zeta^2}$. This results in the staggered phase pattern with tunable $\phi = \tan^{-1}\zeta$. The NN coupling along $\Delta\mathbf{r}_y$ can

[§]In principle, exact physical separations between trapped atoms do not play a significant role with photon-mediated long-range interactions. One may also engineer the spin Hamiltonian based on atoms sparsely trapped along a photonic crystal, even without specific ordering. It is only necessary to map the underlying symmetry and dimensionality of the desired spin Hamiltonian onto the physical system.

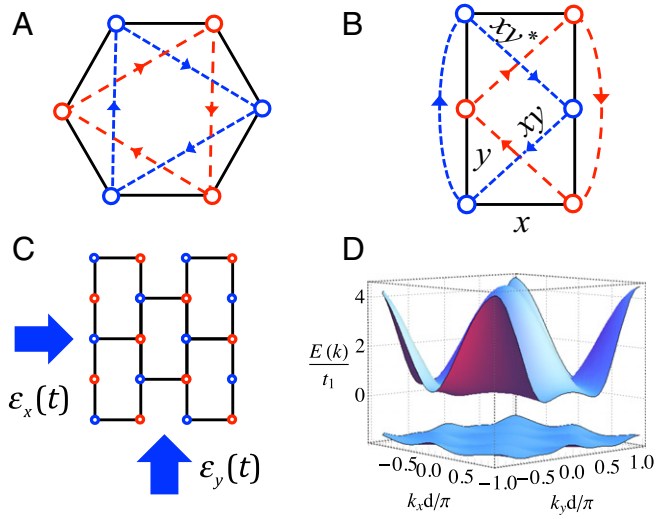


**Fig. 7.** Engineering a honeycomb-equivalent topological brick wall lattice. (*A*) Unit cell of a honeycomb lattice. Solid lines mark the NN hopping. Dashed lines mark the NNN hopping with phase gain $\phi$ along the direction of the arrows. (*B*) Unit cell of a brick wall lattice. Solid lines indicate the NN hopping as in *A*. NNNN hopping (curved dashed lines) and NNN hopping (diagonal dashed lines) correspond to the complex NNN hopping in *A*, making the two models topologically equivalent. (*C*) Brick wall lattice. Filled arrows illustrate the pump electric fields. (*D*) Band structure of the brick wall lattice, plotted with $\cos\phi = 3\sqrt{3/43}$ (58).

be introduced via another sideband with detuning $\tilde{\omega}_y = \delta_y = |\mu_B \nabla B \cdot \Delta\mathbf{r}_y|$ and $X_y(\mathbf{r}_n + \Delta\mathbf{r}_y) = -(|\Omega_1|/2\Delta)\,[e^{-i(n_y+1)\pi} + i\zeta e^{-in_x\pi}]$.

***NNN coupling along*** $\Delta\mathbf{r}_{\alpha=xy,xy^*}$. The sign of the coefficient depends on the sublattices. To engineer these couplings, we use two sidebands formed by field components in $\varepsilon_x(t)$, with detunings $\delta_{\alpha=xy,xy^*}$ and $X_\alpha(\mathbf{r}_n + \Delta\mathbf{r}_{xy,xy^*}) = \pm(|\Omega_2|/2\Delta)e^{-i\pi(n_x+1)}$ at NNN sites. After pairing with the pump field $X_0$ at site $\mathbf{r}_n$, the resulting exchange coefficients are $J_{m,n} = \tilde{J}X_0 X^*_{\alpha=xy,xy^*} = \mp t_2(-1)^{n_x-n_y}$, forming the required pattern with $t_2 = \tilde{J}|X_0||X_{xy}|$.

***NNNN coupling along*** $2\Delta\mathbf{r}_{\alpha=x,y}$. We use two sidebands $X_{2x,2y} = |\Omega_3|e^{-i\pi n_y}/2\Delta$, propagating along $\hat{y}$ with detunings $2\delta_{\alpha=x,y}$, to introduce the real coupling coefficient $t_3 = \tilde{J}|X_0||X_{2x}|$.

Summing up, all of the components in the Raman field can be introduced by merely two pump beams propagating along $\hat{x}$ and $\hat{y}$ directions, respectively. In *SI Appendix C: Pump Field Configurations for Engineering a Chiral-Flux Square Lattice Model*, we explicitly write down the time-dependent electric field that contains all of the sidebands.

We note that it is also possible to simultaneously introduce both blue-detuned ($\delta_\alpha > 0$) and red-detuned ($\delta_{-\alpha} = -\delta_\alpha$) sidebands in the Raman field to control the same spin-exchange term. That is, $J_{m,n} = \tilde{J}[X_0(\mathbf{r}_n)X^*_\alpha(\mathbf{r}_m) + X^*_0(\mathbf{r}_m)X_{-\alpha}(\mathbf{r}_n)]$, which has contributions from $X_\alpha$ and $X_{-\alpha}$ of blue and red sidebands, respectively. Arranging both sidebands with equal amplitudes lead to equal contributions in the engineered coupling coefficient. This corresponds to applying amplitude modulations in the pump electric field. In real experiments, amplitude modulation can be achieved by, for example, the combination of acoustic-optical modulators, and optical IQ-modulators.

**"Honeycomb"-Equivalent Topological Lattice Model.** To further demonstrate the flexibility of the proposed platform, we create Haldane's honeycomb model (73) via a topologically equivalent brick wall lattice (74, 86). Here, we engineer the brick wall configuration using the identical atom–PCW platform discussed in the previous example. Mapping between the two models is illustrated in Fig. 7 *A* and *B*, which contains the following two nontrivial steps: (*i*) generating a checkerboard-like NN-exchange pattern in the $\hat{x}$ direction; (*ii*) obtaining NNN (along $\Delta\mathbf{r}_{xy,xy^*}$) and NNNN (along $2\Delta\mathbf{r}_y$) couplings with the same strength and with a coupling phase $\phi_{mn} = \pm\phi$, which alternates sign across two sublattices. Thus, our target Hamiltonian is given by the following:

$$H = t_1 \sum_{\langle m,n\rangle} (\sigma^\dagger_m \sigma_n + \text{h.c.}) + t_2 \sum_{\{m,n\}} (e^{i\phi_{mn}} \sigma^\dagger_m \sigma_n + \text{h.c.}), \qquad [17]$$

where $\langle . \rangle$ denotes NN pairs in the brick wall configuration (Fig. 7) and $t_1$ is the coupling coefficient. Note that, for simplicity, we discuss a special case where all NN-coupling coefficients from a brick wall vertex are identical. The second summation in Eq. **17** runs over both NNN and NNNN pairs with identical coupling coefficient $t_2$ and alternating phase $\phi_{mn} = \pm\phi$ (Fig. 7).

As in the previous case, we use a strong pump field (propagating along $\hat{y}$), as well as several other weak sidebands to generate all necessary spin-exchange terms. Detailed descriptions on engineering individual terms can be found in *SI Appendix D: Pump Field Configurations for Engineering a Topological Spin Model in a Brick Wall Lattice*. The most important ingredient, discussed here, is that we can generate checkerboard-like NN coupling (along $\hat{x}$), with $J_{m,n} = \tilde{J}X_0 X^*_x = (t_1/2)[1-(-1)^{n_x-n_y}]$. This is achieved by using a sideband of detuning $\delta_x$ and amplitude $X_x = (|\Omega|/4\Delta)[e^{-in_y\pi} + \zeta e^{-i(n_x+1)\pi}]$ at position $\mathbf{r}_m = \mathbf{r}_n + \Delta\mathbf{r}_x$, formed by two fields propagating along $\hat{y}$ and $\hat{x}$, respectively. If both fields have the same amplitude ($\zeta = 1$), they either add up or cancel completely depending on whether $n_x - n_y$ is odd or even. If one applies the same trick toward NN coupling along $\hat{y}$, but with $\zeta \neq 1$, the coupling amplitude modulates spatially in a checkerboard pattern. Essentially, all three NN terms around a brick wall vertex can be independently controlled, opening up further possibilities to engineer, for example, Kitaev's honeycomb lattice model (87, 88).

For physical implementations, again only two pump beams can introduce all components required in the Raman field, which is very similar to the previous case. We stress that, by merely changing the way the Raman field is modulated, one can dynamically adjust the engineered spin Hamiltonians and even the topology, as we compare both cases. This is a unique feature enabled by our capability to fully engineer long-range spin interactions.

Moreover, many of the tricks discussed above can also be implemented in 1D PCWs. It is even possible to engineer a topological 1D spin chain, by exploiting long-range interactions to map out nontrivial connection between spins. For example, our method can readily serve as an realistic approach to realize a topological 1D spin chain as recently proposed in ref. 89.

***XXZ*** **Spin Hamiltonian with Tunable Interaction** $1/r^\eta$. In the last example, we highlight the possibility of engineering a large class of *XXZ* spin Hamiltonians, which were studied extensively in the literature because of the emergence of frustration related phenomena (60, 90–96) and their intriguing nonequilibrium dynamics (45–50). An *XXZ* Hamiltonian is typically written as follows:

$$H_{XXZ} = -B\sum_n \sigma^z_n + \sum_{n<m} \frac{J}{r^\eta_{n,m}} \left[\cos(\theta)\sigma^z_n\sigma^z_m + \sin(\theta)\left(\sigma^x_n\sigma^x_m + \sigma^y_n\sigma^y_m\right)\right], \qquad [18]$$

where an effective magnetic field $B$ controls the number of excitations, $r_{m,m} = |\mathbf{r}_n - \mathbf{r}_m|$, and the parameter $\theta$ determines the relative strength between the *ZZ* and *XY* interactions. This class of spin models has been previously studied, but mostly restricted to nearest neighbors (90–93) or dipolar ($\eta = 3$) interactions (60, 94, 95).

In our setup, one can simulate *XXZ* models with arbitrary $\eta$ by first introducing unique ground-state energy shifts at each of the separation $\mathbf{r}_n - \mathbf{r}_m$, and then applying a strong pump field of amplitude $\Omega_0$ together with $N_d$ auxiliary fields $\Omega_\alpha$ of different detunings

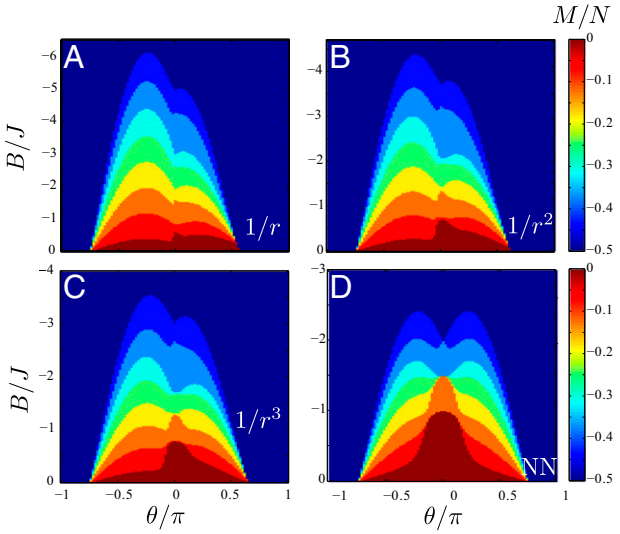


**Fig. 8.** Mean magnetization $M/N$ for a system with $N=16$ atoms in a square lattice, restricted to $N_{\text{exc}} \leq 8$ excitations and $\eta=1$ (*A*), 2 (*B*), 3 (*C*), and NN couplings (*D*).

to introduce spin interactions at each separations.[¶] Moreover, the parameter $\theta$ that determines the ratio between $ZZ$ and $XY$ interaction can be controlled by using different pump intensities in the stroboscopic steps (*SI Appendix E: PCW and Pump Field Configurations for Engineering an XXZ Spin Hamiltonian with $1/r^{\eta}$ Interaction*).

To illustrate physics that can emerge in the first experimental setups with only a few atoms, we study the total magnetization of a small square lattice of $n_s \times n_s$ (=$N$) 16 atomic spins. We apply exact diagonalization restricting to $N_{\text{exc}} \leq 8$ excitations for $N=16$ spins and cover one-half of the phase diagram with $B>0$. In Fig. 8, we explore the mean magnetization of the system $M/N = \frac{1}{2}\sum_i^N \langle \sigma_i^z \rangle / N$ as a function of $B$ and $\theta$ for $\eta=1$ (*A*), 2 (*B*), 3 (*C*), and NN couplings (*D*). At $\theta=0$, the system behaves classically showing the so-called "devil staircase" (97) of insulating states with different rational filling factors and crystalline structures. As already explored in ref. 95 for 1D dipolar systems ($\eta=3$), the presence of long-range interactions, compared with nearest-neighbor models, lead to stronger frustration effects. This manifests in the magnetization diagram with an asymmetry between $\theta \lessgtr 0$. In Fig. 8, we show that longer-range interactions lead to even higher degree of asymmetry. Moreover, in refs. 60 and 95, it was discussed that long-range coupling leads to the formation of supersolid phases, in which crystalline structure and long-range order coexist. These may be even more favored by longer-range interactions. Full characterization of the phases diagram is, however, beyond the scope of this paper and will be discussed elsewhere.

Another especially interesting arena is the behavior of strongly long-range interacting systems ($\eta$ smaller than the lattice dimension $D$) under nonequilibrium dynamics. It has recently been predicted to yield "instantaneous" transmission of correlations after a local quench (45, 47, 48, 96), breaking the so-called Lieb-Robinson bound.

Finally, it is interesting to point out that magnetization can be measured by first freezing the interaction (via shutting off the pump lasers) followed by atom number counting using state-dependent fluorescence imaging. Coherence and off-diagonal long-range orders of the many-body states may be probed via guided photons in another propagation mode along the PCW (98).

**Limitations and Error Analysis.** Until now, we have mainly focused on how to engineer $H_0$ in an ideal situation. We neglected spontaneous emission or GM photon losses and considered that the energy gradient (or $\delta$, the ground-state energy difference between nearest neighboring atoms) can be made very large compared with the interaction energy scales that we want to simulate ($|\delta| \gg |J_{m,m+1}|$). Because the effect of finite cooperativities was considered in detail in refs. 36 and 37, and their conclusions translate immediately to our extension to multifrequency pumps, in this work we mainly focus on the effect of finite $\delta$. In addition, we also discuss the effects of AC Stark shifts as in Eq. **9**, and its error contributions, together with other possible error sources.

**Corrections Introduced from Higher Harmonics: A Floquet Analysis.** We discuss errors and the associated error reduction scheme following a Floquet analysis with multifrequency driving (99, 100), applicable mainly to 1D models. Including all of the time-dependent terms in a multifrequency pumping scheme, we have (Eq. **5**) $H(t) = \sum_p H_p e^{ip\delta t}$, where $H_p$ represents the part that oscillates at frequency $p\delta$. This Hamiltonian has a period $T = 2\pi/\delta$. It can be shown that at integer multiples of $T$, the observed system should behave as if it is evolving under an effective Hamiltonian[#]:

$$H_{\text{eff},1} \approx H_0 + \frac{1}{\delta}\sum_p \frac{[H_p, H_{-p}]}{p} + \frac{1}{2\delta^2}\sum_p \frac{[[H_p,H_0],H_{-p}] + [[H_{-p},H_0],H_p]}{p^2}. \quad [19]$$

This means that the leading error in our simple scheme would be on the order of $J^2/\delta$, where $J$ is the simulated interaction strength. However, we note that if $H_p = \pm H_{-p}$, the leading error term $\sum_p [H_p, H_{-p}]/(p\delta)$ should vanish. In other words, first-order error vanishes if $H_p$ is either symmetric or antisymmetric under a time reversal operation $\mathscr{T}$. Although the original Hamiltonian $H(t)$ does not necessarily possess such symmetry, it is possible to introduce a two-step periodic operation $H_{2\text{step}} = \{H, \mathscr{T}H, H, \mathscr{T}H, \dots\}$ to cancel the first-order error while keeping the time-independent part $H_{2\text{step},0} = H_0$ identical. This results in an effective Hamiltonian in the Floquet picture:

$$H_{\text{eff},2} = H_0 + H_{\text{err},2} \approx H_0 + \frac{4}{\delta^2}\sum_p (-1)^p \frac{[[\tilde{H}_p, H_0], \tilde{H}_p]}{p^2}, \quad [20]$$

where $\tilde{H}_p$ is the (operator) Fourier coefficient of the two-step Hamiltonian and the leading error reduces to the order of $J^3/\delta^2$.

To achieve the time reversal operation, we must reverse the phase of the driving lasers, as well as the sign of the energy offsets between the atoms. Specifically, we can engineer a periodic two-step Hamiltonian by first making the system evolve under presumed $H_0$ (along with other time-dependent terms) for a time interval $T$, and then, for the next time interval $T$, we flip the sign of the energy gradient, followed by reversing the propagation direction of the Raman fields such that $X_\alpha \to X_\alpha^*$ in Eq. **5**. As a result, all of the time-dependent Hamiltonians $H_p$, $\forall p \neq 0$, become $H_{-p}$ in the second step, resulting in $\tilde{H}_p = (-1)^p \tilde{H}_{-p}$ required for error reduction; whereas the time-independent Hamiltonian $H_0$ remains identical in the two-step Hamiltonian. See *SI Appendix F: Error Reduction and Analysis* for more discussions.

[¶]To simulate a square lattice of $n_s \times n_s$ (=$N$) atomic spins, we find that the number of different distances grows as $N_d = (n_s(n_s+1)-2)/2$, which is linearly proportional to the number of atoms $N_d \propto N$.

[#]When the measurement time is incommensurate with period $T$, small-amplitude and fast-oscillating spin-dynamics due to time-dependent terms in Eq. **5** manifest as extra errors; see the discussion about micromotion in refs. 99 and 100.

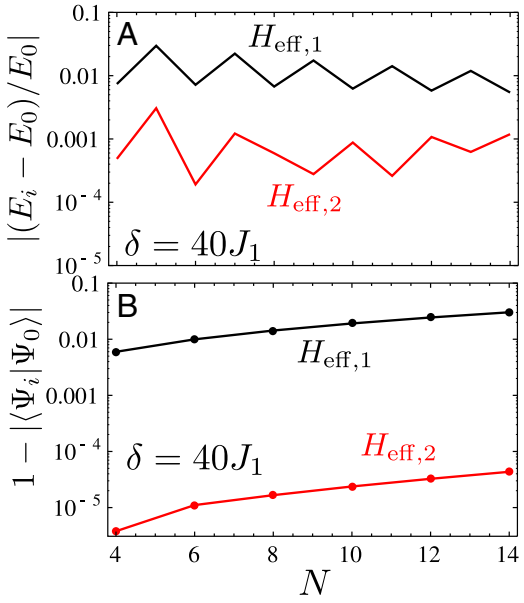


**Fig. 9.** (*A*) Comparison of ground-state energy error $|(E_0 - E_i)/E_0|$ and (*B*) ground-state overlap $|\langle\Psi_0|\Psi_i\rangle|$ as a function of $N$ for Hamiltonians $H_{\mathrm{eff},1}$ (black) and $H_{\mathrm{eff},2}$ (red) with detuning $\delta/J_1 = 40$.

**Numerical Analysis on the Haldane–Shastry Spin Chain.** We now analyze numerically and discuss error on one particular example. For numerical simplicity, we choose the Haldane–Shastry model as its 1D character makes it numerically more accessible. However, the conclusions regarding the estimation of errors can be mostly extended to other models. As we have shown in Eq. **13**, the Haldane–Shastry Hamiltonian is composed by an $XY$ term plus a $ZZ$ term that we can simulate stroboscopically. As we already analyzed the Trotter error due to the stroboscopic evolution, here we focus on the $XY$ part of the Hamiltonian, which reads as follows:

$$H_{\mathrm{HS,xy}} = \sum_{m=1}^{N}\sum_{n=1}^{N-m} \frac{J_0}{\sin^2(n\pi/N)}\left(\sigma_{sg}^{m}\sigma_{gs}^{m+n} + \sigma_{sg}^{m+n}\sigma_{gs}^{m}\right), \qquad [21]$$

where $J_0 = J\pi^2/N^2$. Following the prescribed engineering steps, the total time-dependent Hamiltonian resulting from multiple sidebands can be written as $H(t) = \sum_p H_p e^{ip\delta t}$, with the following:

$$H_p = \sum_{m=1}^{N}\sum_{n=1}^{N-m}\left(J_{n,(p)}\sigma_{sg}^{m}\sigma_{gs}^{m+n} + J_{n,(-p)}^{*}\sigma_{sg}^{m+n}\sigma_{gs}^{m}\right), \qquad [22]$$

and we have defined $J_{n,(p)} = \sum_{\alpha,\beta=0}^{N-1} X_\alpha X_\beta^{*}\delta_{n-p,\beta-\alpha}$. Here, $X_\alpha$ are fixed such that $H_0 = H_{\mathrm{HS,xy}}$.

To illustrate the effect of error cancellations, we consider first a scenario where we directly apply Eq. **22**. To leading order, the effective Hamiltonian is $H_{\mathrm{eff},1}$ as in Eq. **19**. We then analyze the two-step driving, using the effective Hamiltonian $H_{\mathrm{eff},2}$ in Eq. **20**, with $\tilde{H}_p$ given by Eqs. **S45** and **S46**.

We calculate the ground-state energies and eigenvectors of $H_0$, $H_{\mathrm{eff},1}$, and $H_{\mathrm{eff},2}$, which we denote as $E_{0,1,2}$ and $|\Psi_{0,1,2}\rangle$, respectively, for different number of atoms and different ratios of $\delta/J_0$. The results are shown in Figs. 9 and 10. In panels *A*, we show the error in absolute value with respect to the ideal Hamiltonian $H_0$. Interestingly, due to particular structure of $|\Psi_0\rangle$ and $H_p$, one can show that $\langle\Psi_0|[H_p, H_{-p}]|\Psi_0\rangle \approx 0$ and the first-order correction to the energy vanishes. This is confirmed in Fig. 10*A*, where we found that the error actually scales with $1/\delta^2$.

Moreover, it is also enlightening to compare the overlap of the ground states as shown in Figs. 9*B* and 10*B*. We only compute the even-atom number configuration as the odd ones are degenerate and therefore the ground state is not uniquely defined. We see that the ground-state overlap of $H_{\mathrm{eff},2}$ is several orders of magnitude better than the one with $H_{\mathrm{eff},1}$. Moreover, its dependence on $\delta$ is better than the $1/\delta^2$ expectation.

**The Role of Time-Dependent Stark Shifts in the Error Analysis.** In the previous discussions, we have dropped the contribution of the time-dependent Stark shifts:

$$H_{\mathrm{ac}}(t) = -\sum_{n}\sum_{\alpha>\beta}^{m_P-1}\Re\left[\frac{\Omega_\alpha\Omega_\beta^{*}}{2\Delta}e^{i\tilde{\omega}_{\alpha\beta}t}\right]\sigma_{ss}^{n}, \qquad [23]$$

where $\tilde{\omega}_{\alpha,\beta} = \tilde{\omega}_\alpha - \tilde{\omega}_\beta$. In *SI Appendix F: Error Reduction and Analysis*, we discuss its role in the effective Hamiltonian, using the Floquet error analysis. To summarize, we evaluated the error in the two-step driving scheme in various configurations.

***Generic Hamiltonians with translational invariance.*** By translational invariance, we mean that there are no site-dependent spin interactions, and the spin-exchange coefficients remain identical as we offset the spin index by one or more. This means that all components in the pump field should drive the system with uniform optical phases as in the Haldane–Shastry model discussed above. The error by $H_{ac}(t)$ averages out to zero in the Floquet picture. In the butterfly scheme, however, both $|g\rangle$ and $|s\rangle$ states are pumped and they may be shifted differently. This leads to slight modifications in the engineered $XX$ and $YY$ terms.

***Models containing sublattices.*** For topological models that contain sublattices, as in our examples, the pump fields are not perfectly transverse and Stark shifts are site dependent, resulting in nonvanishing error. For realistic PCW realizations, one should set moderate pump detuning $J/\Delta \gtrsim O(1)$ such that leading error contribution will be $\lesssim J^3/\delta^2$, and for $\delta \gg J$, the Stark shift terms may be ignored.

***Stark shift-dominated regime.*** It may be possible that our sublattice models be purposely driven with large-amplitude pumps such that $|\Omega|^2/\Delta \gtrsim \delta$. Stark shift contributions would become important in the resulting spin dynamics. However, if we choose a large pump

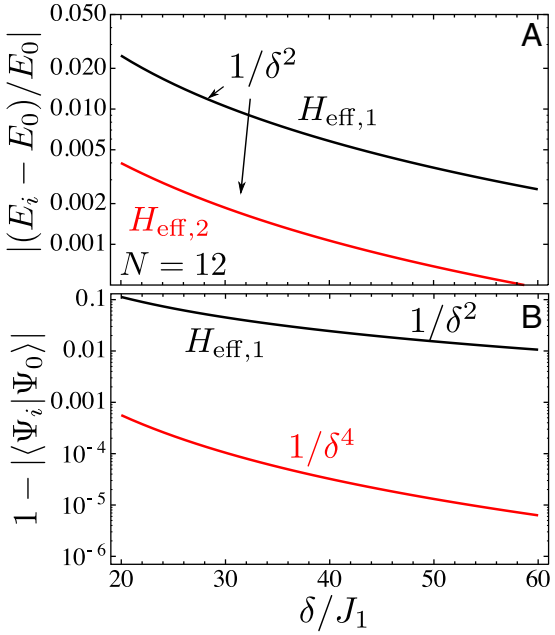


**Fig. 10.** (*A*) Comparison of ground-state energy error $|(E_0 - E_i)/E_0|$ and (*B*) ground-state overlap $|\langle\Psi_0|\Psi_i\rangle|$ as a function of $\delta/J_1$ for Hamiltonians $H_{\mathrm{eff},1}$ (black) and $H_{\mathrm{eff},2}$ (red) for $N = 12$ atoms.

detuning $\Delta > \tilde{J}$, the dominant error contribution can in fact be written in the following simple form:

$$H_{\mathrm{err},2} \approx \sum_{m,n} \tilde{A}_{m,n} \left( J_{m,n} \sigma_{gs}^{m} \sigma_{sg}^{n} + h.c. \right), \qquad [24]$$

where $\tilde{A}_{m,n}$ is a site-dependent amplitude. In a special case that only two sublattices are present, as in our examples, we note that $\tilde{A}_{m,n}$ may only depend on the distance $r_{m,n}$ and is site independent. This "error" term would then uniformly modify the $XY$ coupling strengths to a new value:

$$J'_{m,n} = \left(1 + \tilde{A}_{m,n}\right) J_{m,n}. \qquad [25]$$

The next leading order errors are a factor of $\sim \tilde{J}/\Delta$ smaller than this leading Stark shift contribution, suggesting we can always increase the detuning $\Delta$, while keeping $|\Omega|/\Delta$ constant, to reduce the error contribution.

**Other Error Sources and Heating Effects.** Apart from errors arising from multifrequency driving, there are other common error sources in cold atoms that we have not considered so far, such as motional heating. In the PCW platform, atoms are tightly confined with a trap depth more than three orders of magnitude larger than the recoil energy, rendering well-separated motional bands such that effects like interband heating (101) can be suppressed. Spin-exchange rates in the PCW platform, however, can be adjusted to 1 MHz $\gtrsim |J^{xy,z}| \gg 1$ kHz so that the many-body time scales ($\ll 1$ ms) can be much faster than those associated with motional heating.

In fact, spin temperature can be decoupled from real atomic temperature while simulating the spin models. For example, one can polarize atomic spins initially in a strong magnetic field ($B \gg |J^{xy,z}|$) to approximate a zero-temperature paramagnetic phase (17). The magnetic field can then be ramped down adiabatically to the final value of the desired spin model. Limitations to adiabaticity and, therefore, to the accessible spin temperature will ultimately be limited by the fidelity of the spin-exchange (36, 37) or by motional heating that leads to dephasing, whichever gives a more stringent bound.

## Conclusions and Outlook

In this paper, we have shown that atom-nanophotonic systems present appealing platforms to engineer many-body quantum matter by using low-dimensional photons to mediate interaction between distant atom pairs. We have shown that, by introducing energy gradients in 1D and 2D, and by applying multifrequency Raman addressing beams, it is possible to engineer a large class of many-body Hamiltonians. In particular, by carefully arranging the propagation phases of Raman beams, it is possible to introduce geometric phases into the spin system, thereby realizing nontrivial topological models with long-range spin–spin interactions.

Another appealing feature of our platform is the possibility of engineering periodic boundary conditions, as explicitly shown in the 1D Haldane–Shastry model, or other global lattice topology by introducing long-range interactions between spins located at the boundaries of a finite system. Using 2D PCWs, for example, it is possible to create previously unavailable spin-lattice geometries such as Möbius strip, torus, or lattice models with singular curvatures such as conic geometries (102) that may lead to localized topological states with potential applications in quantum computations.

We emphasize that all of the pairwise-tunable interactions can be dynamically tuned via, for example, electro-optical modulators at timescales much faster than that of characteristic spin interactions. Therefore, the spin interactions can either be adiabatically adjusted to transform between spin models or even be suddenly quenched down to zero by removing all or part of the Raman coupling beams. We may monitor spin dynamics with great detail: after we initially prepare the atomic spins in a known state by, say, individual or collective microwave addressing, we can set the system to evolve under a designated spin Hamiltonian, followed by removing all of the interactions to "freeze" the dynamics for atomic state detection. Potentially, this allows for detailed studies on quantum dynamics of long-range, strongly interacting spin systems that are driven out-of-equilibrium. The dynamics may be even richer because the spins are weakly coupled to a structured environment via photon dissipations. We expect such a platform may bring novel opportunities to the study of quantum thermalization in long-range many-body systems, or for further understanding of information propagation in a long-range quantum network.

**ACKNOWLEDGMENTS.** We gratefully acknowledge discussions with T. Shi and Y. Wu. The work of C.-L.H. and H.J.K. was funded by the Institute for Quantum Information and Matter, a National Science Foundation (NSF) Physics Frontier Center with support of the Moore Foundation; by the Air Force Office of Scientific Research (AFOSR) Quantum Memories in Photon-Atomic Solid-State Systems Multidisciplinary Research Program of the University Research Initiative (MURI); by the Department of Defense National Security Science and Engineering Faculty Fellowship Program; by NSF Grant PHY1205729; by the Office of Naval Research (ONR) Award N00014-16-1-2399; and by the ONR Quantum Opto-Mechanics with Atoms and Nanostructured Diamond MURI. A.G.-T. and J.I.C. acknowledge funding by the European Union integrated project "Simulators and Interfaces with Quantum Systems." A.G.-T. also acknowledges support from Alexander Von Humboldt Foundation and Intra-European Marie Curie Fellowship Nanophotonics for Quantum Information and Simulation (625955).

1. Cirac JI, Zoller P (2012) Goals and opportunities in quantum simulation. *Nat Phys* 8(4): 264–266.
2. Jaksch D, Zoller P (2005) The cold atom Hubbard toolbox. *Ann Phys* 315(1):52–79.
3. Bloch I, Dalibard J, Nascimbène S (2012) Quantum simulations with ultracold quantum gases. *Nat Phys* 8:267–276.
4. Trotzky S, et al. (2008) Time-resolved observation and control of superexchange interactions with ultracold atoms in optical lattices. *Science* 319(5861):295–299.
5. Simon J, et al. (2011) Quantum simulation of antiferromagnetic spin chains in an optical lattice. *Nature* 472(7343):307–312.
6. Greif D, Uehlinger T, Jotzu G, Tarruell L, Esslinger T (2013) Short-range quantum magnetism of ultracold fermions in an optical lattice. *Science* 340(6138): 1307–1310.
7. Griesmaier A, Werner J, Hensler S, Stuhler J, Pfau T (2005) Bose-Einstein condensation of chromium. *Phys Rev Lett* 94(16):160401.
8. Lu M, Burdick NQ, Youn SH, Lev BL (2011) Strongly dipolar Bose-Einstein condensate of dysprosium. *Phys Rev Lett* 107(19):190401.
9. Micheli A, Brennen G, Zoller P (2006) A toolbox for lattice-spin models with polar molecules. *Nat Phys* 2(5):341–347.
10. Ni KK, et al. (2008) A high phase-space-density gas of polar molecules. *Science* 322(5899):231–235.
11. Yan B, et al. (2013) Observation of dipolar spin-exchange interactions with lattice-confined polar molecules. *Nature* 501(7468):521–525.
12. Jaksch D, et al. (2000) Fast quantum gates for neutral atoms. *Phys Rev Lett* 85(10): 2208–2211.
13. Weimer H, Muller M, Lesanovsky I, Zoller P, Buchler HP (2010) A Rydberg quantum simulator. *Nat Phys* 6(5):382–388.
14. Saffman M, Walker TG, Mølmer K (2010) Quantum information with Rydberg atoms. *Rev Mod Phys* 82(3):2313–2363.
15. Schauß P, et al. (2012) Observation of spatially ordered structures in a two-dimensional Rydberg gas. *Nature* 491(7422):87–91.
16. Porras D, Cirac JI (2004) Effective quantum spin systems with trapped ions. *Phys Rev Lett* 92(20):207901.
17. Kim K, et al. (2010) Quantum simulation of frustrated Ising spins with trapped ions. *Nature* 465(7298):590–593.
18. Blatt R, Roos CF (2012) Quantum simulations with trapped ions. *Nat Phys* 8(4): 277–284.
19. Britton JW, et al. (2012) Engineered two-dimensional Ising interactions in a trapped-ion quantum simulator with hundreds of spins. *Nature* 484(7395):489–492.
20. Islam R, et al. (2013) Emergence and frustration of magnetism with variable-range interactions in a quantum simulator. *Science* 340(6132):583–587.
21. Korenblit S, et al. (2012) Quantum simulation of spin models on an arbitrary lattice with trapped ions. *New J Phys* 14(9):095024.
22. Kimble HJ (2008) The quantum internet. *Nature* 453(7198):1023–1030.
23. Baumann K, Guerlin C, Brennecke F, Esslinger T (2010) Dicke quantum phase transition with a superfluid gas in an optical cavity. *Nature* 464(7293):1301–1306.
24. Gopalakrishnan S, Lev BL, Goldbart PM (2009) Emergent crystallinity and frustration with Bose–Einstein condensates in multimode cavities. *Nat Phys* 5(11):845–850.
25. Goban A, et al. (2014) Atom-light interactions in photonic crystals. *Nat Commun* 5:3808.

26. Goban A, et al. (2015) Superradiance for atoms trapped along a photonic crystal waveguide. *Phys Rev Lett* 115(6):063601.
27. Thompson JD, et al. (2013) Coupling a single trapped atom to a nanoscale optical cavity. *Science* 340(6137):1202–1205.
28. Tiecke TG, et al. (2014) Nanophotonic quantum phase switch with a single atom. *Nature* 508(7495):241–244.
29. Majumdar A, et al. (2012) Design and analysis of photonic crystal coupled cavity arrays for quantum simulation. *Phys Rev B* 86(19):195312.
30. Javadi A, et al. (2015) Single-photon non-linear optics with a quantum dot in a waveguide. *Nat Commun* 6:8655.
31. Barclay PE, Fu KM, Santori C, Beausoleil RG (2009) Hybrid photonic crystal cavity and waveguide for coupling to diamond NV-centers. *Opt Express* 17(12):9588–9601.
32. Hausmann BJM, et al. (2013) Coupling of NV centers to photonic crystal nanobeams in diamond. *Nano Lett* 13(12):5791–5796.
33. Houck AA, Türeci HE, Koch J (2012) On-chip quantum simulation with superconducting circuits. *Nat Phys* 8(4):292–299.
34. Eichler C, et al. (2015) Exploring interacting quantum many-body systems by experimentally creating continuous matrix product states in superconducting circuits. *Phys Rev X* 5(4):041044.
35. McKay DC, Naik R, Reinhold P, Bishop LS, Schuster DI (2015) High-contrast qubit interactions using multimode cavity QED. *Phys Rev Lett* 114(8):080501.
36. Douglas JS, et al. (2015) Quantum many-body models with cold atoms coupled to photonic crystals. *Nat Photonics* 9(5):326–331.
37. González-Tudela A, Hung CL, Chang D, Cirac J, Kimble H (2015) Subwavelength vacuum lattices and atom-atom interactions in photonic crystals. *Nat Photonics* 9(5):320–325.
38. Kurizki G (1990) Two-atom resonant radiative coupling in photonic band structures. *Phys Rev A* 42(5):2915–2924.
39. John S, Wang J (1990) Quantum electrodynamics near a photonic band gap: Photon bound states and dressed atoms. *Phys Rev Lett* 64(20):2418–2421.
40. John S, Wang J (1991) Quantum optics of localized light in a photonic band gap. *Phys Rev B Condens Matter* 43(16):12772–12789.
41. Hartmann MJ, Brandao FGSL, Plenio MB (2006) Strongly interacting polaritons in coupled arrays of cavities. *Nat Phys* 2(12):849–855.
42. Greentree AD, Tahan C, Cole JH, Hollenberg LCL (2006) Quantum phase transitions of light. *Nat Phys* 2(12):856.
43. Cho J, Angelakis DG, Bose S (2008) Fractional quantum Hall state in coupled cavities. *Phys Rev Lett* 101(24):246809.
44. Hartmann MJ, Brandão FGSL, Plenio MB (2008) Quantum many-body phenomena in coupled cavity arrays. *Laser Photonics Rev* 2(6):527.
45. Eisert J, van den Worm M, Manmana SR, Kastner M (2013) Breakdown of quasilocality in long-range quantum lattice models. *Phys Rev Lett* 111(26):260401.
46. Gong ZX, Foss-Feig M, Michalakis S, Gorshkov AV (2014) Persistence of locality in systems with power-law interactions. *Phys Rev Lett* 113(3):030602.
47. Jurcevic P, et al. (2014) Quasiparticle engineering and entanglement propagation in a quantum many-body system. *Nature* 511(7508):202–205.
48. Richerme P, et al. (2014) Non-local propagation of correlations in quantum systems with long-range interactions. *Nature* 511(7508):198–201.
49. Hazzard KRA, et al. (2014) Quantum correlations and entanglement in far-from-equilibrium spin systems. *Phys Rev A* 90(6):063622.
50. Vodola D, Lepori L, Ercolessi E, Gorshkov AV, Pupillo G (2014) Kitaev chains with long-range pairing. *Phys Rev Lett* 113(15):156402.
51. Jaksch D, Zoller P (2003) Creation of effective magnetic fields in optical lattices: The Hofstadter butterfly for cold neutral atoms. *New J Phys* 5(1):56.
52. Bermudez A, Schaetz T, Porras D (2011) Synthetic gauge fields for vibrational excitations of trapped ions. *Phys Rev Lett* 107(15):150501.
53. Kolovsky AR (2011) Creating artificial magnetic fields for cold atoms by photon-assisted tunneling. *EPL* 93(2):20003.
54. Aidelsburger M, et al. (2013) Realization of the Hofstadter Hamiltonian with ultracold atoms in optical lattices. *Phys Rev Lett* 111(18):185301.
55. Miyake H, Siviloglou GA, Kennedy CJ, Burton WC, Ketterle W (2013) Realizing the Harper Hamiltonian with laser-assisted tunneling in optical lattices. *Phys Rev Lett* 111(18):185302.
56. Haldane FDM (1988) Exact Jastrow-Gutzwiller resonating-valence-bond ground state of the spin-(1/2 antiferromagnetic Heisenberg chain with $1/r^2$ exchange. *Phys Rev Lett* 60(7):635–638.
57. Shastry BS (1988) Exact solution of an $S = 1/2$ Heisenberg antiferromagnetic chain with long-ranged interactions. *Phys Rev Lett* 60(7):639–642.
58. Neupert T, Santos L, Chamon C, Mudry C (2011) Fractional quantum Hall states at zero magnetic field. *Phys Rev Lett* 106(23):236804.
59. Sun K, Gu Z, Katsura H, Das Sarma S (2011) Nearly flatbands with nontrivial topology. *Phys Rev Lett* 106(23):236803.
60. Maik M, Hauke P, Dutta O, Zakrzewski J, Lewenstein M (2012) Quantum spin models with long-range interactions and tunnelings: A quantum Monte Carlo study. *New J Phys* 14(11):113006.
61. Blais A, Huang RS, Wallraff A, Girvin SM, Schoelkopf RJ (2004) Cavity quantum electrodynamics for superconducting electrical circuits: An architecture for quantum computation. *Phys Rev A* 69(6):062320.
62. Schuster DI, et al. (2007) Resolving photon number states in a superconducting circuit. *Nature* 445(7127):515–518.
63. Jané E, Vidal G, Dür W, Zoller P, Cirac JI (2003) Simulation of quantum dynamics with quantum optical systems. *Quantum Inf Comput* 3(1):15–37.
64. Berry DW, Ahokas G, Cleve R, Sanders BC (2007) Efficient quantum algorithms for simulating sparse Hamiltonians. *Commun Math Phys* 270(2):359–371.
65. Childs AM, Kothari R (2011) Simulating sparse Hamiltonians with star decompositions. *Theory of Quantum Computation, Communication, and Cryptography* (Springer, Berlin), pp 94–103.
66. Berry DW, Childs AM (2012) Black-box Hamiltonian simulation and unitary implementation. *Quantum Information and Computation* 12(1-2):29.
67. Dalibard J, Gerbier F, Juzeliūnas G, Öhberg P (2011) Colloquium: Artificial gauge potentials for neutral atoms. *Rev Mod Phys* 83(4):1523–1543.
68. Hauke P, et al. (2012) Non-abelian gauge fields and topological insulators in shaken optical lattices. *Phys Rev Lett* 109(14):145301.
69. Struck J, et al. (2013) Engineering Ising-xy spin-models in a triangular lattice using tunable artificial gauge fields. *Nat Phys* 9(11):738–743.
70. Goldman N, Juzeliūnas G, Öhberg P, Spielman IB (2014) Light-induced gauge fields for ultracold atoms. *Rep Prog Phys* 77(12):126401.
71. Atala M, et al. (2014) Observation of chiral currents with ultracold atoms in bosonic ladders. *Nat Phys* 10(8):588–593.
72. Kennedy CJ, Burton WC, Chung WC, Ketterle W (2015) Observation of Bose-Einstein condensation in a strong synthetic magnetic field. *Nat Phys* 11(10):859–864.
73. Haldane FDM (1988) Model for a quantum Hall effect without Landau levels: Condensed-matter realization of the "parity anomaly." *Phys Rev Lett* 61(18):2015–2018.
74. Jotzu G, et al. (2014) Experimental realization of the topological Haldane model with ultracold fermions. *Nature* 515(7526):237–240.
75. Duca L, et al. (2015) An Aharonov-Bohm interferometer for determining Bloch band topology. *Science* 347(6219):288–292.
76. Aidelsburger M, et al. (2015) Measuring the chern number of Hofstadter bands with ultracold bosonic atoms. *Nat Phys* 11(2):162–166.
77. Fläschner N, et al. (2016) Experimental reconstruction of the Berry curvature in a topological Bloch band. *Science* 352(6389):1901–1094.
78. Lohse M, Schweizer C, Zilberberg O, Aidelsburger M, Bloch I (2016) A thouless quantum pump with ultracold bosonic atoms in an optical superlattice. *Nat Phys* 12(4):350–354.
79. Nakajima S, et al. (2016) Topological thouless pumping of ultracold fermions. *Nat Phys* 12(4):296–300.
80. Wu Z, et al. (2015) Realization of two-dimensional spin-orbit coupling for Bose-Einstein condensates. arXiv:1511.08170.
81. Mancini M, et al. (2015) Observation of chiral edge states with neutral fermions in synthetic Hall ribbons. *Science* 349(6255):1510–1513.
82. Stuhl BK, Lu HI, Aycock LM, Genkina D, Spielman IB (2015) Visualizing edge states with an atomic Bose gas in the quantum Hall regime. *Science* 349(6255):1514–1518.
83. Cooper NR, Dalibard J (2013) Reaching fractional quantum Hall states with optical flux lattices. *Phys Rev Lett* 110(18):185301.
84. Yao NY, et al. (2013) Realizing fractional Chern insulators in dipolar spin systems. *Phys Rev Lett* 110(18):185302.
85. Wang YF, Gu ZC, Gong CD, Sheng DN (2011) Fractional quantum Hall effect of hard-core bosons in topological flat bands. *Phys Rev Lett* 107(14):146803.
86. Tarruell L, Greif D, Uehlinger T, Jotzu G, Esslinger T (2012) Creating, moving and merging Dirac points with a Fermi gas in a tunable honeycomb lattice. *Nature* 483(7389):302–305.
87. Kitaev A (2006) Anyons in an exactly solved model and beyond. *Ann Phys* 321(1):2–111.
88. Feng XY, Zhang GM, Xiang T (2007) Topological characterization of quantum phase transitions in a spin-1/2 model. *Phys Rev Lett* 98(8):087204.
89. Graß T, Muschik C, Celi A, Chhajlany RW, Lewenstein M (2015) Synthetic magnetic fluxes and topological order in one-dimensional spin systems. *Phys Rev A* 91(6):063612.
90. Wessel S, Troyer M (2005) Supersolid hard-core bosons on the triangular lattice. *Phys Rev Lett* 95(12):127205.
91. Melko RG, et al. (2005) Supersolid order from disorder: Hard-core bosons on the triangular lattice. *Phys Rev Lett* 95(12):127207.
92. Boninsegni M, Prokof'ev N (2005) Supersolid phase of hard-core bosons on a triangular lattice. *Phys Rev Lett* 95(23):237204.
93. Trefzger C, Menotti C, Lewenstein M (2008) Ultracold dipolar gas in an optical lattice: The fate of metastable states. *Phys Rev A* 78(4):043604.
94. Büchler HP, et al. (2007) Strongly correlated 2D quantum phases with cold polar molecules: Controlling the shape of the interaction potential. *Phys Rev Lett* 98(6):060404.
95. Hauke P, et al. (2010) Complete devil's staircase and crystal–superfluid transitions in a dipolar XXZ spin chain: A trapped ion quantum simulation. *New J Phys* 12(11):113037.
96. Hauke P, Tagliacozzo L (2013) Spread of correlations in long-range interacting quantum systems. *Phys Rev Lett* 111(20):207202.
97. Bak P, Bruinsma R (1982) One-dimensional Ising model and the complete devil's staircase. *Phys Rev Lett* 49(4):249–251.
98. Hood JD, et al. (2016) Atom–atom interactions around the band edge of a photonic crystal waveguide. arXiv:1603.02771.
99. Goldman N, Dalibard J (2014) Periodically driven quantum systems: Effective Hamiltonians and engineered gauge fields. *Phys Rev X* 4(3):031027.
100. Goldman N, Dalibard J, Aidelsburger M, Cooper NR (2015) Periodically driven quantum matter: The case of resonant modulations. *Phys Rev A* 91(3):033632.
101. Weinberg M, et al. (2015) Multiphoton interband excitations of quantum gases in driven optical lattices. *Phys Rev A* 92(4):043621.
102. Biswas RR, Son DT (2014) Fractional charge and inter-landau level states at points of singular curvature. arXiv:1412.3809.
103. Gardiner GW, Zoller P (2000) *Quantum Noise* (Springer, Berlin), 2nd Ed.
104. Lloyd S (1996) Universal quantum simulators. *Science* 273(5278):1073–1078.